Journal of Materials Chemistry A

ROYAL SOCIETY OF CHEMISTRY

PAPER

View Article Online
View Journal | View Issue

Cite this: J. Mater. Chem. A, 2026, 14, 8678

Voltage-driven evolution of lithium nanoparticle morphology and SEI precursors

Brad Ayers, [ab] Arihant Bhandari, [abc] Gilberto Teobaldi [d] and Chris-Kriton Skylaris *[ab]

Lithium metal anodes offer unmatched theoretical capacity amongst candidate battery materials, yet their commercial viability remains limited by uncontrolled dendrite growth and solid electrolyte interphase (SEI) formation. Whilst recent work has established that applied voltage controls lithium morphology through potential-dependent surface tension, how voltage determines which electrolyte decomposition products preferentially bind to those evolving surfaces remains unexplored. Here, we employ grand canonical density functional theory with implicit solvation to systematically examine how F^-, O^{2-}, and CO_3^{2-} compete for binding sites across thirteen crystallographic orientations spanning an electrochemically relevant potential window (−1.75 to +1.0 V *vs.* Li/Li^+). Our calculations reveal systematic morphological transitions with decreasing potential: {311} dominates exclusively at +1.0 V, {320} emerges at intermediate potentials, and {110} progressively increases from 30% at −1.0 V to complete dominance at −1.75 V, yielding a rhombic dodecahedron consistent with ultrafast electrodeposition experiments. Competitive adsorption on the thermodynamically dominant surface at each voltage establishes a clear hierarchy: carbonate binding exceeds fluoride by 1.75–2.42 eV throughout the reducing potentials relevant to lithium deposition (−0.5 to −1.75 V), whilst fluoride achieves thermodynamic preference only under oxidising conditions (+1.0 V on {311}). The coupling between morphology and chemistry emerges through surface-dependent site availability—{110} and {311} present 3-fold hollow sites whilst {320} offers 4-fold configurations—which alters binding geometries as voltage drives morphological transitions. These findings rationalise the ubiquitous presence of Li_2CO_3 in experimental SEI characterisation and suggest that achieving LiF-rich interfaces requires kinetic strategies that bypass thermodynamic equilibrium. Our results establish that applied voltage functions as a thermodynamic selector, simultaneously shaping both the structure and composition of the lithium–electrolyte interface.

Received 1st December 2025
Accepted 15th January 2026

DOI: 10.1039/d5ta09820c

rsc.li/materials-a

1 Introduction

Lithium metal anodes represent one of the holy grails of electrochemical energy storage technologies, offering the highest theoretical capacity (3860 mAh g^{-1}) and the lowest electrochemical potential (−3.04V *vs.* SHE) amongst metallic anodes.[1,2] Yet widespread commercial adoption remains fundamentally limited by two intertwined phenomena. The first is the uncontrolled growth of lithium dendrites; ramified structures that propagate through the solvent and electrolyte, leading to capacity fade, safety hazards, and catastrophic cell failure.[1,3] The second is the simultaneous formation of the solid electrolyte interphase (SEI), a passivating film arising from solvent and electrolyte decomposition at the reactive lithium surface.[4] These processes are fundamentally coupled: the SEI mediates ion transport to the growing surface, whilst the evolving morphology determines which sites are available for said decomposition products to adsorb. Despite this coupling, dendrite suppression[5,6] and SEI optimisation[4] have largely been studied as separate phenomena, leaving the interplay between morphological and chemical evolution poorly understood.

Recent advances have begun to unify this picture from the morphology side. Hagopian *et al.* demonstrated that lithium crystal shape has thermodynamic origins rooted in potential-dependent surface tension,[7] with the densely packed {110} facet remaining stable at moderate overpotentials, whilst other orientations transition toward dendritic growth. Yuan *et al.* provided experimental validation through ultrafast electrodeposition, where SEI formation is kinetically outpaced, revealing intrinsic {110}-faceted rhombic dodecahedra across chemically distinct electrolytes.[8] These findings establish that applied voltage controls which crystallographic surfaces are exposed at the lithium interface.

[a]School of Chemistry, University of Southampton, Highfield, Southampton SO17 1BJ, UK. E-mail: C.Skylaris@soton.ac.uk

[b]The Faraday Institution, Quad One, Becquerel Avenue, Harwell Campus, Didcot, OX110RA, UK

[c]Department of Energy Science and Engineering, Indian Institute of Technology Delhi, Hauz Khas, New Delhi 110016, India

[d]Scientific Computing Department STFC-UKRI, Rutherford Appleton Laboratory, Harwell Campus Didcot OX11 0QX, UK

What remains unclear is how this voltage-driven morphological evolution couples to SEI chemistry. In operating batteries, lithium surfaces are immediately passivated by the SEI; a nanoscale mosaic of decomposition products, typically LiF, Li_2O, and Li_2CO_3, that mediates all subsequent interfacial processes.[4,9–11] Whilst we now have insight into how potential controls which facets dominate the particle surface, equivalent understanding of how electrochemical potential determines which decomposition products preferentially bind to those evolving facets remains absent.

The present work addresses this gap through grand canonical density functional theory with soft-sphere implicit solvation,[12,13] systematically examining how F^-, O^{2-}, and CO_3^{2-} compete for binding sites across an electrochemically relevant potential window (−2.0V to 2.0V *vs.* Li/Li^+). By computing potential-dependent Wulff constructions alongside competitive adsorption energetics, we connect voltage-driven morphological evolution to surface chemistry, providing a thermodynamic framework for how applied potential shapes both the structure and composition of the lithium–electrolyte interface.

2 Methodology

We employed grand canonical density functional theory (GC-DFT) to investigate how applied voltage affects lithium surface morphology and competitive ion adsorption at the interface. This framework enables systematic computation of surface energies, charge distributions, and binding preferences as functions of electrode potential, allowing for direct analysis of the interplay between morphological evolution and adsorption thermodynamics under electrochemical conditions.

2.1 Theoretical framework

Within our GC-DFT framework, the applied electrode potential controls electron transfer at the interface by establishing the system's electronic chemical potential. The equilibrium electron distribution is determined by minimising the grand potential:[13]

$$\Omega = F - \mu_e \cdot Q_{sol} \quad (1)$$

where F is the Helmholtz free energy, μ_e the electron chemical potential, and Q_{sol} the surface charge. This formulation enables direct computation of free energy changes at constant potential, with Q_{sol} serving as the variational parameter responding to the applied potential.

The charge distribution and screening effects at the electrode–electrolyte interface are described through the non-linear Poisson–Boltzmann equation:[14]

$$\nabla\cdot[\varepsilon(r)\nabla\phi(r)] = -4\pi\rho(r) - 4\pi\sum_i c_i z_i e \exp(-\beta z_i e\phi(r)) \quad (2)$$

where $\varepsilon(r)$ is the position-dependent dielectric permittivity, $\phi(r)$ the electrostatic potential, $\rho(r)$ the charge density of the electrode, c_i the bulk concentration of ionic species i, z_i the ionic charge number, e the elementary charge, and $\beta = 1/(k_B T)$ the inverse thermal energy.

For each crystallographic orientation, the surface energy/tension, γ was calculated using:

$$\gamma(U) = \frac{E_{slab}(U) - \eta E_{bulk}}{2A} \quad (3)$$

where $E_{slab}(U)$ represents the potential-dependent total energy of the slab, η the ratio of atoms in the slab to the bulk, E_{bulk} the total energy of bulk lithium, and A the surface area. Under electrochemical conditions, the applied potential U introduces an additional degree of freedom such that $\gamma(n\hat{o},U) = \gamma 0(n\hat{o}) + \Delta\gamma(n\hat{o},U)$, where $\gamma 0(n\hat{o})$ is the potential-independent surface energy, $n\hat{o}$ the outward surface normal direction, and $\Delta\gamma(n\hat{o},U)$ arises from potential-dependent surface charging. Different crystallographic orientations exhibit anisotropic responses to applied potential, leading to voltage-dependent modifications of the equilibrium crystal morphology.

The equilibrium morphology of crystalline materials is governed by the minimisation of surface free energy. Following Wulff's theorem,[15,16] the equilibrium crystal shape is constructed by plotting the surface energy $\gamma(n\hat{o})$ as a function of the surface normal direction $n\hat{o}$ to create a polar γ-plot. For each direction, a plane perpendicular to $n\hat{o}$ is drawn at distance $\gamma(n\hat{o})$ from the origin. The inner envelope of all such planes defines the equilibrium crystal morphology, satisfying the relationship $h_i/\gamma_i = \lambda$ (constant), where h_i is the perpendicular distance from the crystal centre to facet i (Fig. 1). For lithium metal electrodes, we observe a transition from {110}-dominated morphology at −1.0 V *vs.* Li^+/Li to {311}-dominated morphology at +0.5 V, demonstrating significant potential-induced restructuring of the exposed facet distribution.

For voltage-dependent adsorption calculations, we extended this framework by computing binding energies as:

$$E_{ads}(U) = E_{slab+ion}(U) - E_{slab} - E_{ion}^{ref} \quad (4)$$

where the potential dependence enters through the adsorbate–substrate system ($E_{slab+ion}(U)$). This captures how the evolving surface charge distribution under applied potential alters binding preferences for F^-, O^{2-}, and CO_3^{2-} ions.

2.2 Computational details

All calculations were performed using the Quantum ESPRESSO package,[17] utilising the Environ module[18] to account for implicit solvent and electrolyte effects. Exchange-correlation effects were treated using the Perdew–Burke–Ernzerhof (PBE) functional,[19] whilst ultrasoft pseudopotentials from the Standard Solid-State Pseudopotentials (SSSP) library[20] described the electron–ion interactions. The Kohn–Sham wave functions were expanded in a plane-wave basis set with kinetic energy and charge density cutoffs of 40 Ry and 600 Ry, respectively. Brillouin zone sampling employed a Monkhorst–Pack k-point mesh with 0.10 $Å^{-1}$ spacing, with cold smearing (0.01 Ry width) aiding electronic convergence.

For surface calculations, we constructed slabs using the Pymatgen library,[21] incorporating all low-index surfaces up to Miller index {332}. Each slab surface energy was converged with respect to the number of layers, with a 20 Å vacuum region to prevent periodic image interactions. Structures were optimised

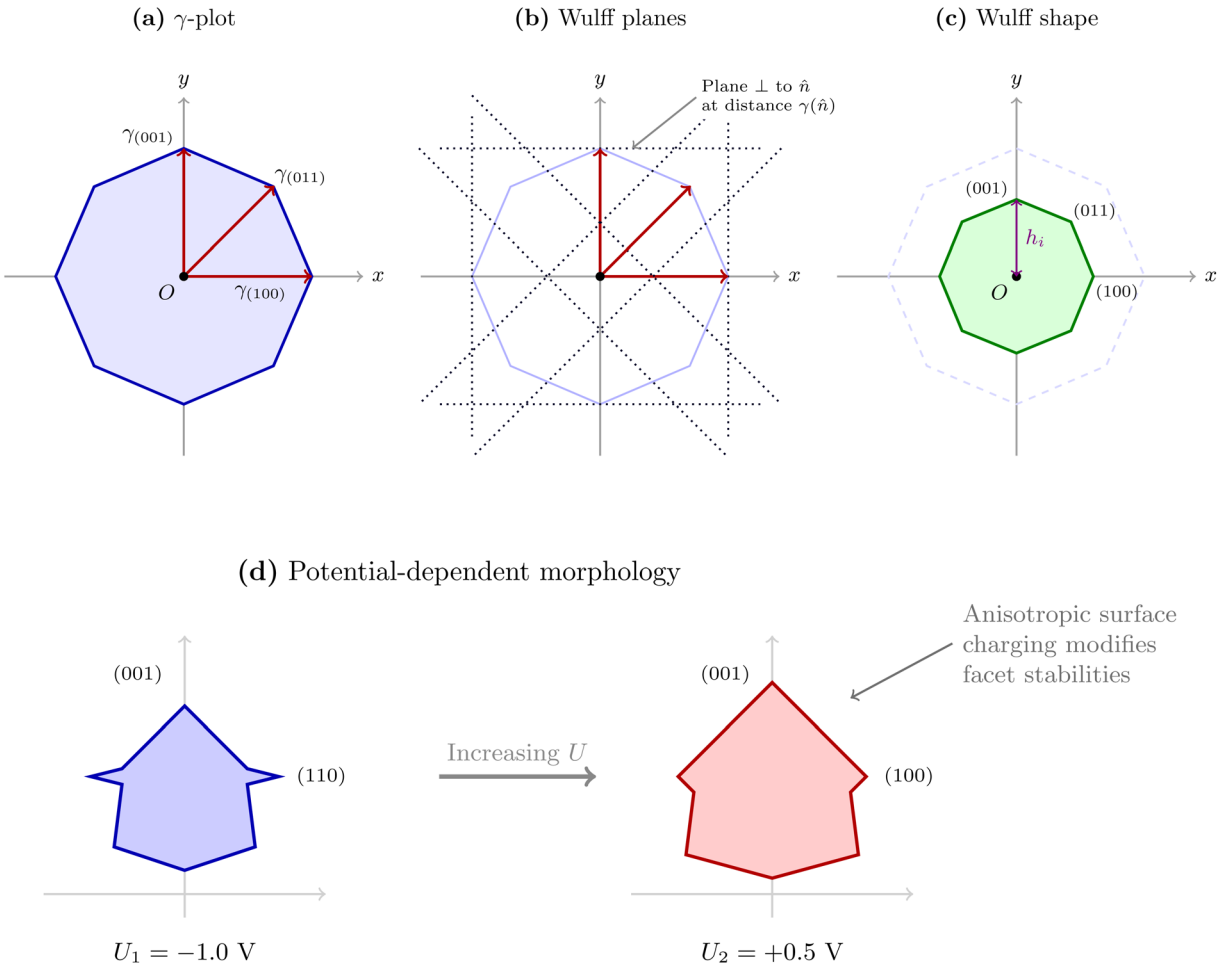

Fig. 1 Wulff construction for equilibrium crystal morphology. (a) The γ-plot represents surface energy as a function of crystallographic orientation. (b) Wulff planes are constructed perpendicular to each surface normal $n\hat{o}$ at distance $\gamma(n\hat{o})$ from the origin. (c) The equilibrium crystal shape is the inner envelope of all Wulff planes, with facet distances satisfying $h_i/\gamma_i = \lambda$. (d) Under electrochemical conditions, applied potential U modifies surface energies anisotropically, leading to voltage-dependent morphological evolution.

until residual forces on atoms fell below 4.0×10^{-4} Ry/bohr ($\approx$0.01 eV Å^{-1}) and total energy differences reached 1.0×10^{-5} Ry between geometry steps.

The electrochemical interface was modelled using a 1 M concentration of symmetric +1:−1 ions to represent $LiPF_6$ in ethylene carbonate at 298.15 K. The solvent was described through a continuum dielectric model with static permittivity of 89.9 and surface tension of 37.3 dyn cm^{-1}. We employed the Fisicaro soft-sphere solvent model,[12] utilising lithium's Bondi radii[22] scaled by 1.32; a factor that minimised mean absolute errors for both lithium-ion solvation energies and experimental capacitance values (5–20 μF cm^{-2}).[23–25] The electrostatic problem was solved with convergence tolerances of $10^{-15}e$ Ry and $10^{-20}e$ Ry for outer and inner loop iterations, respectively, incorporating parabolic corrections for periodic boundary conditions.

The absolute potential of the lithium reference electrode used within this study was constructed *via* a Born–Haber cycle following Trasatti's approach:[26]

$$Li^+(solv.) + e^-(vac.) \rightarrow Li(s) + p.e. \quad (5)$$

The standard reduction potential of lithium was obtained by dividing the Helmholtz free energy change by the charge transferred ($-e$):

$$\varepsilon^{Li^+/Li} = \frac{\Delta F}{-e} = F_{Li}(s) - F_{Li^+}(solv.) + F_{p.e.} \quad (6)$$

where F^+_{Li}(solv.) is obtained from a single Li-ion calculation in a solvated environment, $F_{p.e.}$ represents the energy of the pure electrolyte in the simulation cell, and F_{Li}(s) is the energy of bulk lithium metal.

Surface energies were computed across a voltage range from −2.0 to +2.0 V *vs.* Li^+/Li in 0.5 V increments, providing comprehensive coverage of electrochemically relevant conditions. Wulff constructions were limited to potentials where at least one surface energy remained positive, as negative surface energies indicate thermodynamically unstable conditions favouring spontaneous surface expansion.

For the competitive adsorption studies, we examined F^-, O^{2-}, and CO_3^{2-} binding at all symmetry-distinct sites (on-top, bridge, 3-fold, and 4-fold) on the area-dominant surfaces at their corresponding voltages within the range −1.75 to +1.0 V *vs.*

Li^+/Li; these being the voltages at which surface energies remain positive ($\gamma > 0$). Adsorbate structures were generated using the Automated Catalysis Adsorption Toolkit (ACAT) and treated with D3-BJ[27,28] dispersion correction and a marginally higher force threshold of 1×10^{-3} Ry/bohr (≈ 0.025 eV Å^{-1}).[29] This systematic approach reveals how crystallographic orientation and applied potential couple to create selective binding environments; a critical factor for understanding initial SEI formation that extends beyond previous morphological studies.

It is important to note that F^-, O^{2-}, and CO_3^{2-} do not exist as free solvated species in the bulk electrolyte; rather, they arise from complex decomposition pathways of the salt and solvent. Our calculations treat these ions as *effective thermodynamic endpoints*, representing the anionic products available for surface binding after decomposition. The computed adsorption energies thus quantify the equilibrium driving forces governing competitive binding (*i.e.*, which species preferentially occupies surface sites given their presence at the interface) rather than predicting the mechanistic pathways by which these species form.

All calculations were executed through a high-throughput computational workflow developed using Parsl[30] and the Atomic Simulation Environment (ASE)[31] packages. This framework enabled parallel computation of both surface energies and adsorption configurations, with automated generation of potential-dependent Wulff constructions and competitive binding analysis.

3 Results

3.1 Solvation effects and equilibrium morphology

Introducing an electrochemical environment induces significant modifications to lithium surface stability. Across all thirteen crystallographically distinct Li surfaces examined, we observe systematic responses when comparing vacuum and solvated conditions.

The calculated potentials of zero charge span a narrow range from −0.745 V for {100} to −0.599 V for {110} *vs.* Li^+/Li, reflecting the different surface dipoles generated for each {hkl} cleavage direction. This potential becomes systematically less negative with increasing surface atomic density. For the bcc lattice, where packing density follows {110} > {100} > {111}, we observe a corresponding trend in potential of zero charge: $PZC_{\{110\}} > PZC_{\{100\}} > PZC_{\{111\}}$.[32,33] This confirms that lithium surfaces maintain net positive charge at the equilibrium potential, with counter-anions preferentially populating the electrical double layer under standard electrochemical conditions.

Most crystallographic orientations experience modest energetic perturbations upon solvation, with Fermi level shifts ranging from −1.004 eV for {111} to −0.411 eV for {110}. The low-index {100} and {110} facets exhibit relatively smaller shifts ($\Delta E_f = -0.565$ and −0.411 eV, respectively), indicating less pronounced electronic reorganisation compared to vacuum. Higher-index surfaces show substantially larger shifts: {111} ($\Delta E_f = -1.004$ eV), {322} ($\Delta E_f = -1.808$ eV), and {332} ($\Delta E_f = -1.816$ eV). This crystallographic anisotropy in solvation response stems from differences in surface corrugation and resultant cavity formation within the implicit solvent model. A complete table of surface energies and solvation-induced changes is provided in the SI (Table S1).

Under vacuum conditions, the predicted equilibrium morphology exhibits substantial contributions from eight facet families (Fig. 2a). The distribution is dominated by three major orientations: {100} at 22.6%, {320} at 22.5%, and {332} at 16.3%, with {310} at 15.1% and {110} at 14.7% making notable contributions. Minor facet families, {311} at 4.0%, {331} at 2.1%, and {221} at 1.8%, account for the remaining surface area. This morphological complexity reflects the near-degeneracy of surface formation energies in vacuum, which span −2.394 to −0.874 eV across the computed orientations.

Implicit solvation fundamentally restructures this facet hierarchy. In the presence of electrolyte (1 M $LiPF_6$ in ethylene carbonate) without applied potential, {332} becomes the dominant orientation at 20.3%, followed by {320} at 17.8%, {100} at 16.8%, {310} at 16.1%, and {210} at 15.5% (Fig. 2b). Notably, the {110} orientation is suppressed to just 2.7%, down from 14.7% in vacuum. This demonstrates that the dielectric environment selectively modulates surface stabilities in a highly anisotropic manner. The emergence of {332} as the dominant facet, rising from 16.3% in vacuum to 20.3% upon solvation, highlights the limitations of vacuum-based studies for electrochemical systems.

The origin of this facet redistribution lies in differential stabilisation of high-index surfaces. Whilst {110} shows a modest Fermi level shift ($\Delta E_f = -0.411$ eV), {332} undergoes a substantially larger perturbation ($\Delta E_f = -1.816$ eV). This preferential stabilisation of corrugated surfaces reflects enhanced cavity formation and electrostatic interactions within the soft-sphere solvent model. The resulting anisotropic energy landscape provides the baseline upon which voltage-dependent transformations occur.

3.2 Voltage-dependent morphological transformation

Applied potential modulates surface energetics through charge accumulation and double–layer interactions. Calculations spanning −2.0 to +2.0 V *vs.* Li^+/Li reveal systematic trends that alter lithium morphology. At oxidising potentials, surface

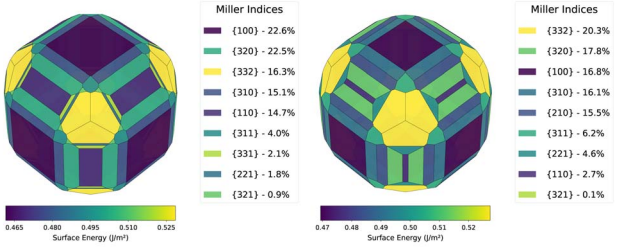

(a) Vacuum (b) Solvated

Fig. 2 Equilibrium Wulff constructions comparing vacuum (a) and solvated (b) environments at zero applied potential. Solvation induces substantial facet redistribution, with {332} becoming dominant at 20.3% and {110} suppressed to 2.7%. Colour scale: 0.47–0.54 J m^{-2}.

energies remain elevated with modest variation between orientations. As the potential shifts negative, a clear divergence emerges: low-index surfaces become preferentially stabilised, driving progressive simplification of the equilibrium morphology.

3.2.1 Oxidising potentials: complex polyhedral morphology. At strongly oxidising conditions (+1.0 V *vs.* Li^+/Li), the morphology transforms to a near-spherical polyhedron composed exclusively of the {311} facet (Fig. 3a). This complete dominance represents a significant shift, as this orientation contributes merely 6.2% under zero-potential solvated conditions. The potential-dependent charging at this voltage uniquely stabilises {311}, which achieves the minimum surface energy of 0.034 J m^{-2} within the calculated range of 0.034–0.517 J m^{-2}.

Decreasing the potential to +0.5 V induces a transition to complex multi-faceted morphology with seven distinct orientations (Fig. 3b). The {320} facet now dominates at 34.1%, with substantial contributions from {311} at 24.2%, {100} at 19.8%, and {332} at 14.9%. Minor facets including {310}, {322}, and {221} collectively account for the remaining 7%. Surface energies span 0.245–0.534 J m^{-2}. The emergence of {320} as the primary facet marks a clear transition away from the {311}-dominated regime observed at higher potentials.

At the equilibrium potential (0.0 V), morphological complexity persists with eight contributing facets (Fig. 3c). The {320} orientation maintains dominance at 38.4%, followed by {100} at 23.1%. The {332}, {311}, {221}, {322}, {310}, and {321} facets collectively constitute the remaining surface area, with individual contributions ranging from 10.9% down to minor percentages. The persistent dominance of {320} suggests particular stability under mild oxidising conditions. This facet distribution differs from the zero-potential solvated case discussed earlier, demonstrating that even modest potential variations induce substantial morphological restructuring.

Beyond +1.0 V, surface energies decrease precipitously, becoming negative above +1.5 V. Negative surface energy ($\gamma < 0$) indicates that the equilibrium Wulff construction becomes invalid; at oxidising potentials, this corresponds to electrochemical dissolution ($Li \rightarrow Li^+ + e^-$), defining the upper voltage boundary for morphological control.

3.2.2 Reductive potentials: progressive simplification and {110} emergence. Under reductive conditions, the morphology evolves systematically towards simpler geometries dominated by the {110} orientation. At moderately reducing potentials (−0.5 V), eight facets contribute to a complex morphology (Fig. 4a). The surface area distribution is relatively balanced: {320} at 25.2%, {310} at 20.4%, {100} at 18.6%, and {332} at 15.2% comprise the major facets. Additional contributions from {221}, {210}, {322}, and {311} account for the remaining area. Surface energies span 0.245–0.514 J m^{-2}, showing modest differentiation between orientations at this potential.

A marked reorganisation occurs at −1.0 V (Fig. 4b). The {110} facet emerges as a co-dominant orientation at 29.7%, nearly matched by {211} at 27.4%. The {310} and {100} facets contribute 20.4% and 13.7% respectively, whilst {320}, {332}, and {111} make minor contributions totalling approximately 9%. This transition demonstrates the emerging preference for the densely-packed {110} surface.

At −1.5 V, the simplification accelerates: {110} now dominates at 59.6% of the total surface area (Fig. 4c). Only three other facets persist: {211} at 23.8%, {100} at 15.9%, and minimal {310} at 0.7%. The overall shape begins to approximate a rhombic dodecahedron. Surface energies span 0.206–0.264 J

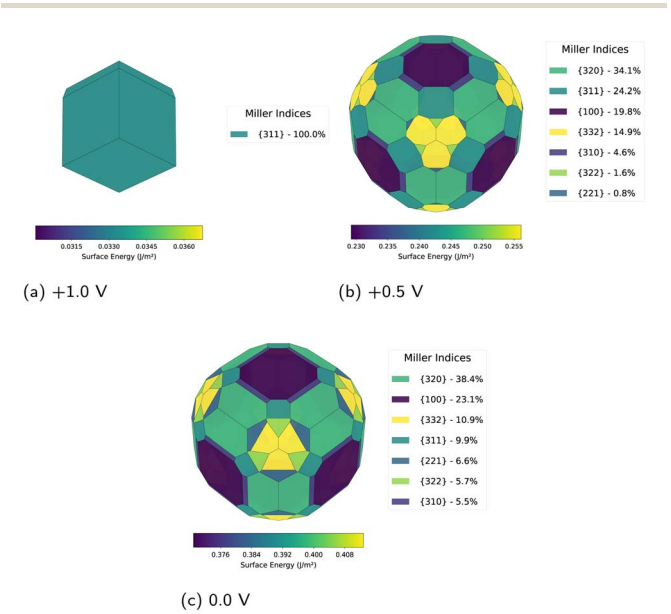

(a) +1.0 V (b) +0.5 V

(c) 0.0 V

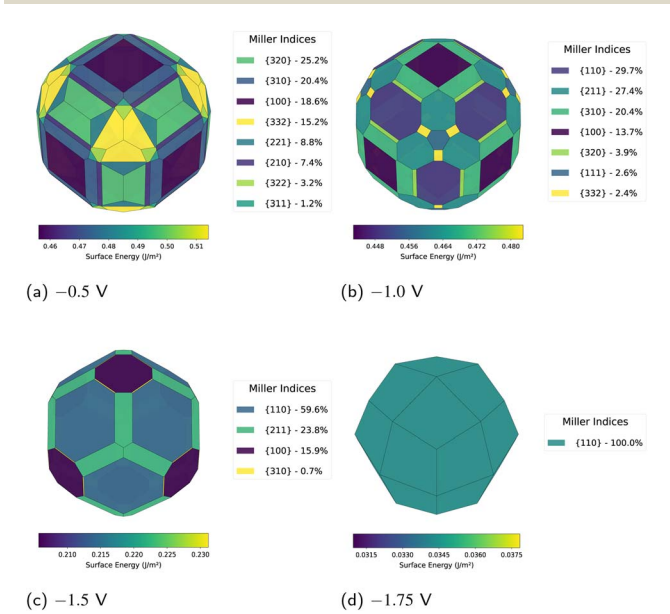

(a) −0.5 V (b) −1.0 V

(c) −1.5 V (d) −1.75 V

Fig. 3 Lithium morphology evolution at oxidising potentials. At +1.0 V (a), the {311} facet dominates exclusively. As potential decreases, complex multi-faceted morphology emerges with {320} becoming dominant at both +0.5 V (b) and 0.0 V (c). Surface energies: 0.23–0.53 J m^{-2}.

Fig. 4 Progressive morphological simplification at reducing potentials demonstrates systematic evolution towards {110} dominance. The {110} contribution increases from 29.7% at −1.0 V (b) to 59.6% at −1.5 V (c), culminating in exclusive expression at −1.75 V (d). This progression aligns with ultrafast electrodeposition experiments.[8]

m^{-2}, representing reductions of 45–59% from the zero-potential reference state. The largest reduction occurs for the {110} orientation, explaining its progressive dominance.

At −1.75 V, the morphological evolution reaches its endpoint: complete {110} dominance yielding a rhombic dodecahedron (Fig. 4d). This represents the final stable configuration before γ becomes negative. At more reducing potentials, surface charge accumulation generates electrostatic repulsions sufficiently strong that creating new surface area to dilute these charges becomes energetically favourable.[7] This marks a transition from surface area minimisation to maximisation, providing the thermodynamic driving force for whisker and dendrite formation observed experimentally. This morphological endpoint aligns with experimental observations from ultrafast electrodeposition studies.[8]

The driving force underlying this transformation lies in differential stabilisation across crystallographic orientations. Whilst all surfaces experience energy reductions at increasingly negative potentials, the effect is stronger for {110}. This facet experiences a 59% energy reduction compared to 45–50% for other orientations. The preferential stabilisation arises from the lower work function of {110}, which enables greater electron accumulation and more favourable electrostatic interactions at negative potentials.

3.3 Implications for morphology-dependent surface chemistry

The voltage-driven facet redistribution establishes a direct connection between applied voltage and the crystallographic orientations exposed at the lithium surface, with implications for SEI formation through distinct adsorption environments.

At typical electrodeposition potentials (−0.5 to −1.5 V), the progressive dominance of {110} suggests that SEI precursors will interact primarily with this orientation. The transition from morphological complexity at −0.5 V, where eight facets contribute meaningfully, to near-exclusive {110} expression at −1.75 V implies that voltage acts as a selector for interfacial chemistry. The systematic evolution of facet distributions, with {110} progressing from 0% at +0.5 V to complete dominance at −1.75 V, provides the foundation for our competitive adsorption studies examining F^-, O^{2-}, and $CO_3{}^{2-}$ species.[34]

Intermediate voltage regimes (−0.5 to −1.0 V) present coexisting facet populations, suggesting intrinsic SEI heterogeneity. During transitions where {110}, {211}, {310}, and {100} all contribute meaningfully to the surface area, orientation-dependent binding preferences may lead to spatially heterogeneous SEI composition. This heterogeneity extends beyond simple electrolyte composition effects, providing insight into the formation of mosaic SEI layers observed experimentally.

3.4 Competitive adsorption of SEI precursors

3.4.1 Thermodynamic framework for SEI component selection. The voltage-dependent morphological evolution established above provides a crystallographic template for solid-electrolyte interphase formation. To investigate the thermodynamic preferences governing interface composition, we examined the competitive adsorption of three primary SEI precursor species: fluoride (F^-), oxide (O^{2-}), and carbonate (CO_32-) ions.[35,36] These species represent the anionic components of the dominant inorganic SEI phases (LiF, Li_2O, and Li_2CO_3) observed in battery post-mortem analysis.[37] As noted in Section 2.2, these ions are treated as effective thermodynamic endpoints; our analysis addresses which species binds preferentially once generated, rather than modelling the decomposition pathways that produce them.

Adsorption calculations were performed on the lowest-energy surface at each voltage, reflecting the thermodynamically dominant facet that SEI precursors would encounter during formation. This approach captures the coupled nature of morphological and chemical evolution: at reducing potentials (−1.75 to −1.0 V) calculations were performed on {110}, at intermediate potentials (−0.5 to +0.5 V) on {320}, and at strongly oxidising conditions (+1.0 V) on {311}. Binding was examined at all symmetry-distinct sites available on each surface. Notably, {110} and {311} surfaces present 3-fold hollow, on-top, and bridge sites, whilst {320} offers 4-fold hollow, on-top, and bridge sites. This difference in site availability means that discontinuities in site preference across the voltage range (Fig. 5) arise from transitions between surfaces rather than site switching on a single facet.

3.4.2 Voltage-dependent binding energetics. Fig. 5 reveals the binding behaviour of each species on the thermodynamically dominant surface at each voltage.The voltage-dependent evolution of the lowest adsorption energies for each species is summarised in Fig. 6, where carbonate (left panel) demonstrates consistently stronger binding than fluoride (centre) and oxide (right) across the entire potential window. Carbonate ions exhibit the strongest adsorption throughout, with binding energies evolving from approximately −10.7 eV at +1.0 V to −9.1 eV at −1.75 V, though intermediate potentials show variation with a minimum around −7.8 eV near −1.0 V. These magnitudes reflect the stabilisation gained when an isolated ion (our reference state) becomes surface-coordinated at the applied bias, incorporating contributions from lithium coordination, charge redistribution, and electrostatic screening within the grand canonical framework. The relative differences between species, which govern competitive binding, remain physically meaningful. This non-monotonic behaviour reflects both the changing surface identity and the competing effects of surface charge accumulation. These magnitudes reflect the stabilisation gained when an isolated ion (our reference state) becomes surface-coordinated at the applied bias, incorporating contributions from lithium coordination, charge redistribution, and electrostatic screening within the grand canonical framework. The relative differences between species, which govern competitive binding, remain physically meaningful.

The preferred binding sites on each surface reveal distinct patterns for each adsorbate. On {311} at +1.0 V, carbonate preferentially occupies on-top sites (−8.241 eV), in contrast to fluoride and oxide which favour higher-coordination 3-fold configurations (−9.028 eV and −7.699 eV, respectively; see Table S3). Transitioning to {320} at intermediate voltages (+0.5 to −0.5 V), 4-fold configurations become available and are

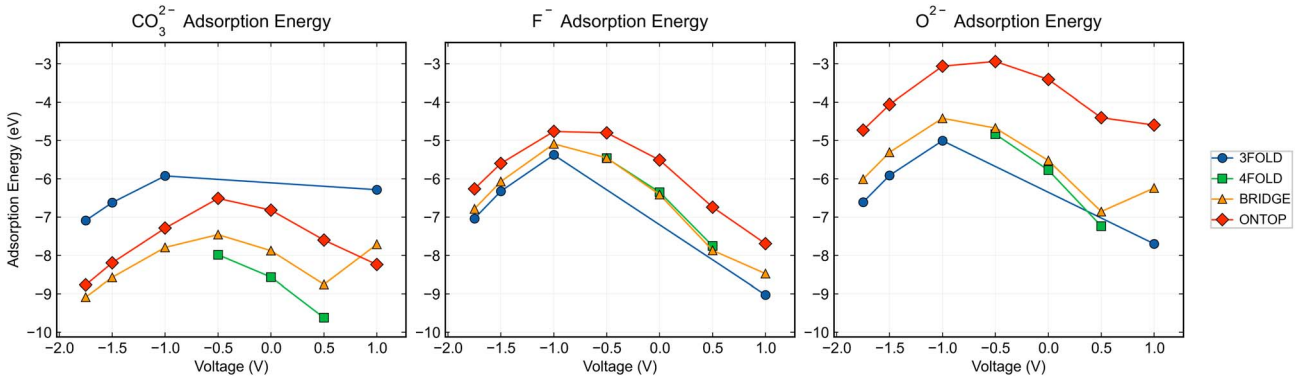

Fig. 5 Voltage-dependent adsorption energies across all symmetry-distinct binding sites. Calculations were performed on the lowest-energy surface at each voltage: {311} at +1.0 V, {320} at +0.5 to −0.5 V, and {110} at −1.0 to −1.75 V. Discontinuities in 3-fold and 4-fold site data reflect transitions between surfaces with different site availability, rather than site-switching behaviour on a single facet.

favoured. At reducing potentials (−1.0 to −1.75 V) where {110} dominates, carbonate settles into bridge sites amongst the available 3-fold, bridge, and on-top options. This progression reflects the interplay between site availability on different surfaces and the electrostatic environment: at reducing potentials, repulsion between the negatively charged carbonate anion and the increasingly negative lithium surface makes lower-coordination bridge sites more favourable than the 3-fold hollows.

Fluoride ions show different preferences across the surface transitions. On {311} at +1.0 V, 3-fold sites are favoured. On {320} at intermediate voltages, bridge configurations dominate near equilibrium before 4-fold sites become preferred approaching −0.5 V. Returning to {110} at reducing potentials, fluoride again occupies 3-fold sites. The binding energies range from −5.4 to −9.0 eV, showing significant sensitivity to both voltage and surface identity. Oxide ions maintain simpler behaviour, preferring 3-fold sites on {311} and {110} at the potential extremes, with 4-fold configurations favoured on {320} near equilibrium. Binding energies fall between −5.0 and −7.6 eV.

3.4.3 Thermodynamic hierarchy and SEI composition. The comparative adsorption analysis reveals voltage-dependent selectivity with implications for SEI composition (Fig. 7). At strongly oxidising conditions (+1.0 V) on {311}, fluoride achieves the strongest binding at −9.03 eV, exceeding carbonate (−8.24 eV) by 0.79 eV. This represents the only potential examined where fluoride demonstrates thermodynamic preference.

This fluoride dominance proves narrow. By +0.5 V on {320}, carbonate binding (−9.62 eV) substantially exceeds fluoride (−7.87 eV) by 1.75 eV. This carbonate preference persists throughout battery-relevant potentials on both {320} and {110} surfaces, with advantages of 2.42 eV at −1.0 V, 2.25 eV at −1.5 V, and 2.05 eV at −1.75 V.

The non-monotonic selectivity has implications for SEI formation. The reduced carbonate advantage near −1.0 V, coinciding with typical lithium deposition potentials and the transition to {110} dominance, suggests a potential window where kinetic factors and concentration gradients might enable mixed SEI composition despite carbonate's thermodynamic preference.[36]

Oxide consistently exhibits the weakest binding across all potentials and surfaces, trailing carbonate by 2.4 to 4.4 eV depending on voltage. This substantial thermodynamic penalty helps explain the relative scarcity of Li_2O in as-formed SEI layers, though it appears in aged interfaces likely through secondary reactions rather than direct competitive adsorption.

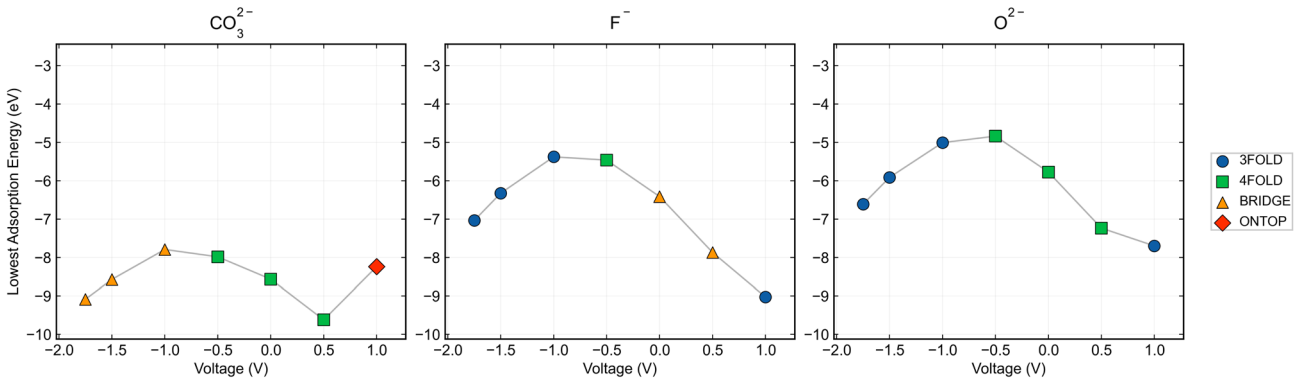

Fig. 6 Voltage-dependent adsorption energies for SEI precursor ions on the lowest-energy lithium surface at each potential. Carbonate (left) demonstrates consistently stronger binding than fluoride (centre) and oxide (right) across the entire potential window. The preferred binding sites reflect both site availability on each surface and electrostatic interactions with the charged electrode.

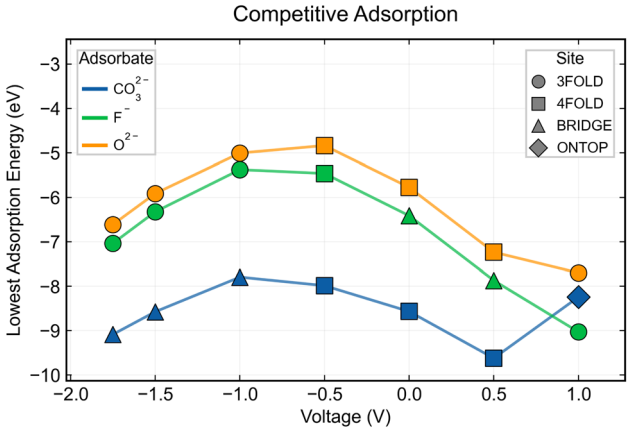

Fig. 7 Comparative adsorption analysis demonstrating the thermodynamic hierarchy amongst SEI precursors. Carbonate maintains a substantial binding advantage across battery-relevant reducing potentials, though the magnitude varies from approximately 1.8 eV at +0.5 V to 2.5 eV near −0.5 V. At strongly oxidising conditions (+1.0 V), fluoride binding becomes thermodynamically preferred.

In real-world battery systems, kinetic factors may override these thermodynamic preferences. Local concentration gradients from salt decomposition, solvent breakdown products, and diffusion limitations could enable fluoride incorporation despite its thermodynamic disadvantage. Additionally, once initial layers form, subsequent adsorption occurs on modified surfaces with different binding characteristics than pristine lithium. Our calculations thus provide insight into initial preferences rather than complete SEI evolution.

This persistent thermodynamic hierarchy explains the ubiquitous presence of Li_2CO_3 in experimental SEI characterisation. Even in fluoride-rich electrolytes from $LiPF_6$ decomposition, carbonate from solvent breakdown dominates due to its stronger surface affinity. Achieving alternative compositions, particularly LiF-rich interfaces, requires kinetic strategies that bypass equilibrium: rapid salt decomposition at high current densities, sacrificial additives that irreversibly form LiF, or preformed artificial SEI layers that prevent direct thermodynamic competition.

The fluoride preference at +1.0 V on {311} offers mechanistic insight. Brief oxidative excursions during cycling could kinetically trap fluoride before subsequent reduction drives carbonate incorporation, though the narrow voltage window and dissolution risks above equilibrium present practical challenges.

3.4.4 Mechanistic implications for SEI architecture. The coupling between surface identity and site preference provides mechanistic insight into SEI structure. At battery-relevant reducing potentials (−1.0 to −1.75 V), carbonate adopts bridge configurations on the dominant {110} surface. Bridge sites offer lower coordination than the 4-fold hollows available on {320} at higher potentials, potentially allowing faster ion exchange and explaining the dynamic nature of the inner SEI layer observed in *operando* studies.[38] The reduced coordination may also facilitate subsequent chemical reactions, as carbonate retains reactive oxygen atoms not fully coordinated to the surface.

The strong binding energies (exceeding −10 eV for carbonate) indicate essentially irreversible adsorption under ambient conditions. These high energies suggest that initial carbonate adsorption creates persistent templates for subsequent SEI growth, with each incorporation permanently consuming lithium and contributing to first-cycle capacity loss.[39]

The transition between surfaces with different site availability suggests that formation protocol, particularly voltage ramping rates and hold potentials, could influence final SEI structure. Holding at intermediate potentials where {320} dominates would present 4-fold sites to incoming adsorbates, whilst rapid transitions to reducing potentials where {110} dominates would expose 3-fold and bridge sites. This provides a potential explanation for the sensitivity of SEI quality to formation conditions beyond simple thickness considerations.

Fluoride's preference for 3-fold sites on both {311} and {110} surfaces, contrasting with carbonate's bridge site preference on {110}, suggests spatial segregation within the SEI matrix. This could contribute to the heterogeneous SEI structure commonly observed, with domains of different composition rather than homogeneous mixing. The weaker fluoride binding also implies greater mobility within the SEI, potentially explaining fluoride enrichment at grain boundaries and defect sites.

3.4.5 Coupling between morphology and chemistry. Our analysis reveals that morphological evolution and chemical selectivity are intrinsically linked through surface identity. The voltage-dependent transition from {311} through {320} to {110} simultaneously determines both the crystallographic template available for SEI growth and the binding sites accessible to decomposition products.

At strongly reducing potentials (−1.5 to −1.75 V) where {110} surfaces dominate, carbonate occupies bridge sites whilst maintaining strong binding. The absence of 4-fold sites on this surface constrains adsorbate geometry, potentially facilitating ordered SEI growth along specific crystallographic directions of the {110} template. Confirming such templating would require explicit surface reaction modelling.

The voltage window of −0.5 to −1.0 V emerges as particularly significant, spanning the transition from {320} to {110} dominance. This morphological transition coincides with a change in available binding sites (loss of 4-fold, gain of 3-fold) and a local minimum in carbonate's binding advantage over fluoride. The convergence of these structural and chemical transitions suggests a critical regime for SEI formation where multiple competing processes occur simultaneously. The reduced thermodynamic driving forces in this window may allow kinetic factors to play larger roles, potentially explaining the variability in SEI composition observed experimentally.[40]

These correlations imply that morphological and chemical evolution cannot be independently controlled. Strategies to modify lithium morphology will inherently affect available binding sites and their relative stabilities, whilst attempts to alter SEI chemistry may feed back to influence surface energetics and morphological evolution. This coupling reinforces the central finding of this work: applied voltage acts not merely as a driving force for electrodeposition, but as a thermodynamic

selector that simultaneously shapes both the structure and composition of the lithium–electrolyte interface.

4 Discussion

4.1 Coupling of morphology and surface chemistry

Applied voltage simultaneously controls both lithium surface morphology and SEI precursor binding through a shared mechanism: voltage-driven transitions between crystallographic orientations. As the potential shifts from oxidising to reducing conditions, the dominant surface evolves from {311} through {320} to {110}, and each surface presents fundamentally different binding sites to decomposition products. Where {110} and {311} offer 3-fold hollow, bridge, and on-top configurations, {320} provides 4-fold sites. Electrochemical potential thus selects not only which facets appear, but which binding geometries become available for initial SEI formation.

This coupling bridges two previously separate areas of lithium metal research. Hagopian *et al.* and Yuan *et al.* established that {110} dominates at reducing potentials,[7,8] whilst SEI characterisation consistently reveals spatially heterogeneous compositions.[11,40] Our results identify voltage-dependent morphological evolution as a potential source of this heterogeneity: as different facets appear and recede during deposition, decomposition products encounter an evolving landscape of binding environments.

4.2 Thermodynamic constraints on SEI composition. Carbonate maintains a persistent thermodynamic advantage over fluoride and oxide throughout battery-relevant potentials. This preference holds on both {320} and {110} surfaces, directly explaining why Li_2CO_3 appears ubiquitously in experimental characterisation[35,37] (even when fluoride-rich electrolytes provide abundant F^- from $LiPF_6$ decomposition).

Fluoride achieves thermodynamic preference only in a narrow oxidative window: +1.0 V on {311}. Whilst this potential exceeds lithium's equilibrium dissolution voltage, it suggests a mechanism worth exploring. Brief oxidative excursions during cycling could kinetically trap fluoride species before subsequent reduction drives carbonate incorporation.[39] The narrow window and dissolution risks present practical challenges, but the persistent carbonate dominance at reducing potentials makes the underlying point clear: achieving LiF-rich interfaces will require kinetic strategies (high current densities, sacrificial additives, or artificial interphases[10]) rather than reliance on intrinsic thermodynamic selectivity.

4.3 Implications for SEI architecture and heterogeneity. Three phenomena converge in the voltage window from −0.5 to −1.0 V: the morphological transition from {320} to {110} dominance, the switch from 4-fold to 3-fold binding sites, and a local minimum in carbonate's energetic advantage over fluoride. This convergence suggests particular sensitivity to formation protocols. The voltage ramp rate through this regime, and any hold potentials within it, may significantly influence final SEI architecture by determining which surfaces dominate during the critical initial deposition stages.

The data also suggest a mechanism for spatial segregation within the SEI. On {110} surfaces that dominate at reducing potentials, carbonate preferentially occupies bridge sites whilst fluoride favours 3-fold hollows. This distinct site selectivity could drive the formation of mosaic structures with compositionally different domains,[4,9] rather than homogeneous mixing. Furthermore, carbonate's preference for lower-coordination bridge sites on {110} (compared to 4-fold hollows on {320}) may facilitate faster ion exchange, consistent with the dynamic inner SEI layer observed in *operando* studies.[38]

From an operational perspective, the critical voltage window of −0.5 to −1.0 V *vs.* Li/Li^+ corresponds to overpotentials of 0.5–1.0 V relative to lithium equilibrium. Whilst our thermodynamic calculations cannot directly predict the current densities at which these potentials are achieved, researchers employing potential-controlled formation protocols or three-electrode configurations can target this regime directly. The convergence of morphological and compositional transitions within this window suggests that formation protocols allowing sufficient equilibration time in this potential range may yield more homogeneous SEI structures than rapid traversal.

4.4 Limitations and broader applicability. Several limitations warrant consideration. Our implicit solvation approach captures dielectric responses and capacitance accurately but excludes specific solvent–molecule interactions and explicit decomposition pathways. Consequently, the high-index plane stabilisation observed in Section 3.1 depends on the dielectric constant of the solvent and the ionic strength of the electrolyte; different parameters may yield quantitatively different facet preferences. The calculations represent thermodynamic endpoints for isolated ions on pristine surfaces, and adsorption was modelled only on the dominant facet at each voltage; minor crystallographic orientations present during multi-faceted growth may exhibit different binding preferences. Operating batteries involve kinetic competition from diffusion barriers, concentration gradients, and nucleation phenomena that may override these thermodynamic preferences.

It is important to note that the present thermodynamic analysis is most directly applicable during the initial stages of SEI formation, when pristine lithium surfaces first interact with electrolyte species and before significant passivation has occurred. During this critical window, competitive adsorption is governed by the equilibrium driving forces computed here, establishing compositional gradients that serve as templates for subsequent SEI development.[39] As the SEI film grows and transitions to kinetic control,[36] factors such as ion transport through existing layers and mechanical constraints become increasingly important.

Explicit modelling of solvent decomposition and surface reactions would clarify whether the crystallographic templating suggested here actually produces ordered SEI growth. Integration with kinetic Monte Carlo methods[36] could bridge the gap between initial adsorption events and long-term interphase evolution, capturing the full complexity of SEI formation under realistic conditions.

The fundamental coupling between surface structure and adsorption thermodynamics likely extends beyond lithium to other metal anode systems (sodium, magnesium, and others) where analogous interphase formation occurs. The broader

implication is straightforward: strategies targeting anode morphology will inevitably alter the binding landscape for electrolyte decomposition. Voltage management protocols should therefore account for these coupled thermodynamic effects rather than treating morphology and chemistry as independent variables.

5 Conclusions

Applied voltage functions as a dual selector in lithium metal batteries, simultaneously controlling both the crystallographic morphology of the anode and the binding preferences of SEI precursors. Through grand canonical density functional theory with implicit solvation, we have established a thermodynamic framework connecting voltage-driven morphological evolution to competitive adsorption at the lithium–electrolyte interface.

The equilibrium morphology undergoes systematic transitions with applied potential: {311} facets dominate at oxidising conditions (+1.0 V), {320} emerges at intermediate potentials, and {110} progressively increases from 30% at −1.0 V to complete dominance at −1.75 V, yielding a rhombic dodecahedron consistent with ultrafast electrodeposition experiments. Each transition fundamentally alters the coordination environments available to adsorbates. Where {320} provides 4-fold hollow sites, {110} offers lower-coordination bridge configurations that become increasingly favourable as surface charge accumulates at reducing potentials.

Competitive adsorption calculations reveal a clear thermodynamic hierarchy. Carbonate binding exceeds fluoride by 1.75 to 2.42 eV throughout the reducing potentials relevant to lithium deposition (−0.5 to −1.75 V), whilst fluoride achieves thermodynamic preference only under oxidising conditions (+1.0 V on {311}). This persistent carbonate advantage directly explains the ubiquitous Li_2CO_3 observed in experimental SEI characterisation, even in fluoride-rich electrolytes. Achieving LiF-rich interfaces may require kinetic strategies (high current densities, sacrificial additives, or artificial interphases) that bypass thermodynamic equilibrium rather than relying on intrinsic selectivity.

The voltage window from −0.5 to −1.0 V emerges as particularly significant, where three phenomena converge: the morphological transition from {320} to {110} dominance, the switch from 4-fold to 3-fold binding sites, and a local minimum in carbonate's energetic advantage. This convergence identifies a critical regime where SEI architecture becomes most sensitive to formation protocols, with voltage ramp rates and hold potentials potentially determining the final interphase composition and structure.

These findings establish that dendrite suppression and SEI engineering are fundamentally coupled through applied voltage. Morphological control inherently determines which binding sites become available to decomposition products, whilst the evolving surface chemistry feeds back to influence subsequent growth. Voltage management thus offers a unified approach to simultaneously shaping both the crystallographic template of the lithium anode and the thermodynamic landscape governing solid-electrolyte interphase formation.

Conflicts of interest

There are no conflicts to declare.

Data availability

Data for this article, including computational input files, output data, surface energy calculations, adsorption energies, and Wulff construction results are available at GitHub at https://github.com/BCAyers2000/li_morphology.git. The repository contains: quantum ESPRESSO and environ input files for all surface and adsorption calculations. Raw computational output data and extracted energies for all thirteen crystallographic orientations across the voltage range −2.0 to +2.0 V *vs.* Li/Li^+. Python scripts for automated calculation workflows using ASE. Analysis scripts and Jupyter notebooks for figure generation. Wulff construction data and facet distribution calculations. Complete adsorption energy datasets for F^-, O_2^-, and CO_3^{2-} on all symmetry-distinct binding sites. Additional supporting data have been provided as part of the supplementary information (SI), including convergence tests, complete surface energy tables, and computational validation results. Supplementary information is available. See DOI: https://doi.org/10.1039/d5ta09820c.

Acknowledgements

BA acknowledges PhD funding from the Scientific Computing Department of STFC. AB and CKS acknowledge Faraday Institution (https://www.faraday.ac.uk/; EP/S 003053/1, grant numbers FIRG084). The calculations presented in this work were performed on the Iridis6 supercomputer at the University of Southampton and the ARCHER2 UK National Supercomputing Service (https://www.archer2.ac.uk; *via* the UKCP HEC EPSRC grant: EP/P022030/1 and EP/X035891/1). We are grateful to the UK Materials and Molecular Modelling Hub for computational resources, which is partially funded by EPSRC (EP/T022213/1, EP/W032260/1 and EP/P020194/1).

Notes and references

1 X.-B. Cheng, R. Zhang, C.-Z. Zhao and Q. Zhang, *Chem. Rev.*, 2017, **117**(15), 10403–10473.
2 W. Xu, J. Wang, F. Ding, X. Chen, E. Nasybulin, Y. Zhang and J.-G. Zhang, *Energy Environ. Sci.*, 2014, **7**(2), 513–537.
3 X.-B. Cheng, R. Zhang, C.-Z. Zhao, F. Wei, J.-G. Zhang, Q. Zhang, X. B. Cheng, R. Zhang, C. Z. Zhao, F. Wei, Q. Zhang and J.-G. Zhang, *Adv. Sci.*, 2016, **3**(3), 1500213.
4 E. Peled, D. Golodnitsky and G. Ardel, *J. Electrochem. Soc.*, 1997, **144**, L208–L210.
5 G. Wan, F. Guo, H. Li, Y. Cao, X. Ai, J. Qian, Y. Li and H. Yang, *ACS Appl. Mater. Interfaces*, 2018, **10**, 593–601.
6 C.-Y. Wang, T. Liu, X.-G. Yang, S. Ge, N. V. Stanley, E. S. Rountree, Y. Leng and B. D. McCarthy, *Nature*, 2022, **611**, 485–490.
7 A. Hagopian, M.-L. Doublet and J.-S. Filhol, *Energy Environ. Sci.*, 2020, **13**, 5186–5197.

8 X. Yuan, B. Liu, M. Mecklenburg and Y. Li, *Nature*, 2023, **620**, 86–91.
9 K. Xu, *J. Power Sources*, 2023, **559**, 232652.
10 T. Li, X.-Q. Zhang, P. Shi and Q. Zhang, *Joule*, 2019, **3**, 2647–2661.
11 H. Adenusi, G. A. Chass, S. Passerini, K. V. Tian and G. Chen, *Adv. Energy Mater.*, 2023, **13**, 2203307.
12 G. Fisicaro, L. Genovese, O. Andreussi, S. Mandal, N. N. Nair, N. Marzari and S. Goedecker, *J. Chem. Theory Comput.*, 2017, **13**, 3829–3845.
13 R. Sundararaman, W. A. Goddard III and T. A. Arias, *J. Chem. Phys.*, 2017, **146**, 114104.
14 S. Ringe, H. Oberhofer, C. Hille, S. Matera and K. Reuter, *J. Chem. Theory Comput.*, 2016, **12**, 4052–4066.
15 G. Wulff, *Z. Kristallogr.*, Vol. 34, 1901, p. 449, References - Scientific Research Publishing, https://www.scirp.org/reference/referencespapers?referenceid=969294.
16 E. Ringe, R. P. Van Duyne and L. D. Marks, *Nano Lett.*, 2011, **11**, 3399–3403.
17 P. Giannozzi, O. Andreussi, T. Brumme, O. Bunau, M. Buongiorno Nardelli, M. Calandra, R. Car, C. Cavazzoni, D. Ceresoli, M. Cococcioni, N. Colonna, I. Carnimeo, A. Dal Corso, S. de Gironcoli, P. Delugas, R. A. DiStasio, A. Ferretti, A. Floris, G. Fratesi, G. Fugallo, R. Gebauer, U. Gerstmann, F. Giustino, T. Gorni, J. Jia, M. Kawamura, H.-Y. Ko, A. Kokalj, E. Küçükbenli, M. Lazzeri, M. Marsili, N. Marzari, F. Mauri, N. L. Nguyen, H.-V. Nguyen, A. Otero-de-la Roza, L. Paulatto, S. Poncé, D. Rocca, R. Sabatini, B. Santra, M. Schlipf, A. P. Seitsonen, A. Smogunov, I. Timrov, T. Thonhauser, P. Umari, N. Vast, X. Wu and S. Baroni, *J. Phys.: Condens. Matter*, 2017, **29**, 465901.
18 O. Andreussi, I. Dabo and N. Marzari, *J. Chem. Phys.*, 2012, **136**.
19 J. P. Perdew, K. Burke and M. Ernzerhof, *Phys. Rev. Lett.*, 1996, **77**, 3865–3868.
20 G. Prandini, A. Marrazzo, I. E. Castelli, N. Mounet and N. Marzari, *npj Comput. Mater.*, 2018, **4**, 72.
21 R. Tran, Z. Xu, B. Radhakrishnan, D. Winston, W. Sun, K. A. Persson and S. P. Ong, *Sci. Data*, 2016, **3**, 160080.
22 A. Bondi, *J. Phys. Chem.*, 1964, **68**, 441–451.
23 I.-T. Kim, M. Egashira, N. Yoshimoto and M. Morita, *Electrochim. Acta*, 2010, **55**, 6632–6638.
24 M. Schalenbach, B. Wu, C.-L. Tsai, A. Windmüller, L. Raijmakers, S. Yu, H. Tempel and R.-A. Eichel, *Energy Adv.*, 2025, **4**, 140–151.
25 N. Legrand, S. Raël, B. Knosp, M. Hinaje, P. Desprez and F. Lapicque, *J. Power Sources*, 2014, **251**, 370–378.
26 S. Trasatti, *Pure Appl. Chem.*, 1986, **58**, 955–966.
27 S. Grimme, J. Antony, S. Ehrlich and H. Krieg, *J. Chem. Phys.*, 2010, **132**, 154104.
28 S. Grimme, S. Ehrlich and L. Goerigk, *J. Comput. Chem.*, 2011, **32**, 1456–1465.
29 S. Han, S. Lysgaard and T. Vegge, Rapid mapping of alloy surface phase diagrams *via* Bayesian evolutionary multitasking, *npj Comput. Mater.*, 2023, **9**, 139.
30 Y. Babuji, A. Woodard, Z. Li, D. S. Katz, B. Clifford, R. Kumar, L. Lacinski, R. Chard, J. M. Wozniak, I. Foster, M. Wilde and K. Chard, *Proceedings of the 28th International Symposium on High-Performance Parallel and Distributed Computing*, New York, NY, USA, 2019, pp. 25–36.
31 A. Hjorth Larsen, J. Jørgen Mortensen, J. Blomqvist, I. E. Castelli, R. Christensen, M. Dułak, J. Friis, M. N. Groves, B. Hammer, C. Hargus, E. D. Hermes, P. C. Jennings, P. Bjerre Jensen, J. Kermode, J. R. Kitchin, E. Leonhard Kolsbjerg, J. Kubal, K. Kaasbjerg, S. Lysgaard, J. Bergmann Maronsson, T. Maxson, T. Olsen, L. Pastewka, A. Peterson, C. Rostgaard, J. Schiøtz, O. Schütt, M. Strange, K. S. Thygesen, T. Vegge, L. Vilhelmsen, M. Walter, Z. Zeng and K. W. Jacobsen, *J. Phys.: Condens. Matter*, 2017, **29**, 273002.
32 M. Jäckle and A. Groß, *J. Chem. Phys.*, 2014, **141**, 174710.
33 F. Faglioni, B. V. Merinov and W. A. I. Goddard, *J. Phys. Chem. C*, 2016, **120**, 27104–27108.
34 Y. Li, Y. Li, A. Pei, K. Yan, Y. Sun, C.-L. Wu, L.-M. Joubert, R. Chin, A. L. Koh, Y. Yu, J. Perrino, B. Butz, S. Chu and Y. Cui, *Science*, 2017, **358**, 506–510.
35 K. Vishweswariah, N. G. Ningappa, M. D. Bouguern, A. Kumar M R, M. B. Armand and K. Zaghib, *Adv. Energy Mater.*, 2025, **15**, 2501883.
36 S. Perez-Beltran, D. Kuai and P. B. Balbuena, *ACS Energy Lett.*, 2024, **9**, 5268–5278.
37 Z. Chen, B. Wang, Y. Li, F. Bai, Y. Zhou, C. Li and T. Li, *ACS Appl. Mater. Interfaces*, 2022, **14**, 28014–28020.
38 G. Feng, H. Jia, Y. Shi, X. Yang, Y. Liang, M. H. Engelhard, Y. Zhang, C. Yang, K. Xu, Y. Yao, W. Xu and X. Shan, *Nat. Nanotechnol.*, 2023, **18**, 780–789.
39 S. Zhang, Y. Li, L. J. Bannenberg, M. Liu, S. Ganapathy and M. Wagemaker, *Sci. Adv.*, 2024, **10**, eadj8889.
40 B. Jagger and M. Pasta, *Joule*, 2023, **7**, 2228–2244.

